



PAPER

PD-ARnet: a deep learning approach for Parkinson's disease diagnosis from resting-state fMRI

To cite this article: Guangyao Li *et al* 2024 *J. Neural Eng.* **21** 056016

View the [article online](#) for updates and enhancements.

You may also like

- [An attention-based multi-modal MRI fusion model for major depressive disorder diagnosis](#)
Guowei Zheng, Weihao Zheng, Yu Zhang et al.
- [Identifying neural correlates of balance impairment in traumatic brain injury using partial least squares correlation analysis](#)
Vikram Shenoy Handiru, Easter Selvan Suviseshamuthu, Soha Saleh et al.
- [DOCTer: a novel EEG-based diagnosis framework for disorders of consciousness](#)
Sha Zhao, Yue Cao, Wei Yang et al.

Breath Biopsy Conference



Join the conference to explore the **latest challenges** and advances in **breath research**, you could even **present your latest work!**



5th & 6th November
Online



Main talks



Early career
sessions



Posters

Register now for free!



PAPER

PD-ARnet: a deep learning approach for Parkinson's disease diagnosis from resting-state fMRI

Guangyao Li¹, Yalin Song^{*} , Mingyang Liang, Junyang Yu and Rui Zhai

Henan Provincial Engineering Research Center of Intelligent Data Processing, Henan University, Kaifeng, Henan, People's Republic of China

¹ First author.^{*} Author to whom any correspondence should be addressed.E-mail: syl@vip.henu.edu.cn**Keywords:** Parkinson's disease, rs-fMRI, deep learning, diagnostic classification**Abstract**

Objective. The clinical diagnosis of Parkinson's disease (PD) relying on medical history, clinical symptoms, and signs is subjective and lacks sensitivity. Resting-state fMRI (rs-fMRI) has been demonstrated to be an effective biomarker for diagnosing PD. **Approach.** This study proposes a deep learning approach for the automatic diagnosis of PD using rs-fMRI, named PD-ARnet. Specifically, PD-ARnet utilizes Amplitude of Low Frequency Fluctuations and Regional Homogeneity extracted from rs-fMRI as inputs. The inputs are then processed through a developed dual-branch 3D feature extractor to perform advanced feature extraction. During this process, a Correlation-Driven weighting module is applied to capture complementary information from both features. Subsequently, the Attention-Enhanced fusion module is developed to effectively merge two types of features, and the fused features are input into a fully connected layer for automatic diagnosis classification. **Main results.** Using 145 samples from the PPMI dataset to evaluate the detection performance of PD-ARnet, the results indicated an average classification accuracy of 91.6% (95% confidence interval [CI]: 90.9%, 92.4%), precision of 94.7% (95% CI: 94.2%, 95.1%), recall of 86.2% (95% CI: 84.9%, 87.4%), F1 score of 90.2% (95% CI: 89.3%, 91.1%), and AUC of 92.8% (95% CI: 91.1%, 95.0%). **Significance.** The proposed method has the potential to become a clinical auxiliary diagnostic tool for PD, reducing subjectivity in the diagnostic process, and enhancing diagnostic efficiency and consistency.

1. Introduction

Parkinson's disease (PD) is the second most common neurodegenerative disease after Alzheimer's disease [1]. However, diagnosing this disease accurately remains a challenging task. A meta-analysis reported misdiagnosis rates of 26.2% among non-specialists and 16.1%–20.4% among specialists [2]. The high misdiagnosis rate of PD stems from the excessive dependence on the patient's motor signs for clinical diagnosis, which are often subtle in the early stages and resemble symptoms of other movement disorders [3]. The pathogenesis of PD is still uncertain, and a complete cure does not exist [4]. Nevertheless, prompt neuroprotective treatment may slow the progression of the disease and potentially

prevent its onset, whereas failure to obtain an accurate diagnosis may accelerate the progression and make it more challenging to control [2, 5, 6]. Hence, accurate diagnosis of PD is crucial for both clinicians and patients.

Resting-state fMRI (rs-fMRI) is a widely used neuroimaging tool that measures spontaneous fluctuations in neural blood oxygen level-dependent (BOLD) signal across the whole brain, and it has been demonstrated to be a useful tool for the diagnosis of PD [7, 8]. Amplitude of Low Frequency Fluctuations (ALFF) and Regional Homogeneity (ReHo) are frequently utilized functional metrics in analyzing rs-fMRI data. They have been shown to have the highest test-retest reliability among rs-fMRI metrics [9]. ALFF visually shows the BOLD signal intensity

of local spontaneous neural activity [10], while ReHo can indicate the synchronization of BOLD signal fluctuations between a given voxel and surrounding voxels [11]. Both methods are widely used to study localized brain activity in neurological diseases. Numerous studies have demonstrated that ALFF and ReHo can reveal manifestations of brain diseases and assist physicians in PD diagnosis [12–14].

Previous studies on PD classification mainly concentrated on the utilization of machine learning methods. For instance, in Shi *et al*'s work, ALFF features were extracted from 246 predefined ROIs, followed by feature selection using a two-sample *t*-test and feature elimination, with SVM ultimately used for PD classification [14]. Cigdem *et al* conducted morphological analysis of sMRI data using VBM, generated 3D gray and white matter masks with a two-sample *t*-test under the *f*-contrast hypothesis, then selected optimal features using LLCFS and the Fisher criterion, and finally detected PD with an SVM classifier [15]. Shi J *et al* extracted MRI features from the pre-defined ROI, then used *t*-test for feature selection, and placed the selected features into the cascade multi-column RVFL+ framework they developed for PD diagnosis [16]. Pang *et al* extracted features from MRI and fMRI data, using *t*-tests and minimum redundancy methods for selection. They then applied empirical kernel mapping to enhance the selected features, feeding them into a cascaded classifier for classification [17]. However, it has been found that there is heterogeneity in different PD datasets [18, 19], which will lead to the lack of repeatability of ROIs across different datasets. Moreover, it is highly likely that manual localized feature selection may overlook features that are potential and crucial to classification.

Compared to machine learning methods, deep learning approaches can automatically perform global feature extraction and minimize the information loss caused by manual feature engineering [20]. In recent years, deep learning has been widely applied to the task of PD diagnosis. For example, Vyas *et al* designed a 3D CNN model that directly operates on MRI data for feature learning and extraction, with the extracted features used for distinguishing PD [21]. Yang *et al* developed a 3D ResNet model, which extracts features from T1-weighted MRI and diagnoses PD through a softmax layer [22]. Yang *et al* proposed a Cross-modal graph neural network that encodes functional and structural connectivity from fMRI and DTI, captures inter-modal dependencies via dynamic graph and mutual learning mechanisms, and uses a bilateral graph Convolutional layer to aggregate multimodal representations for PD detection [23]. In another study, Yang *et al* proposed a self-supervised deep learning framework that pre-trains a brain network Transformer encoder on functional connectivity networks from fMRI data. The encoder extracts feature representations, which

are then classified using an SVM classifier [24]. These studies underscore the critical role of deep learning in advancing PD diagnosis, particularly through the automated feature extraction from MRI or fMRI data, which enhances accuracy and ultimately improves diagnostic outcomes.

Residual network is a type of deep learning neural network architecture proposed by He *et al*, which consists of multiple layers [25]. Through layer-by-layer feature learning, it can automatically learn a series of hierarchical feature representations from the original input data. For ALFF and ReHo data, this hierarchical representation can help the network capture the characteristics of brain functional activity from low-level to high-level. In addition, each layer contains a nonlinear activation function ReLU, which can automatically learn more complex nonlinear patterns. For data with highly nonlinear relationships such as ALFF and ReHo, the deep residual network is helpful for enhancing the effectiveness of feature extraction.

This study aims to develop a deep learning method based on residual networks. This method utilizes ALFF and ReHo for the automatic identification and diagnosis of PD, providing a valuable reference for clinical diagnosis of PD from rs-fMRI data.

2. Materials and methods

The complete flowchart of PD-ARnet is shown in figure 1, consists of three main parts. Firstly, pre-processing of rs-fMRI data is performed, followed by the calculation of ALFF and ReHo. Secondly, ALFF and ReHo inputs are processed by the backbone feature extraction network for automatic feature extraction. During this process, the Correlation-Driven weighting module (CWM) captures complementary information from the two feature branches. Finally, the features experience fusion through the Attention-Enhanced fusion module (AFM), and the fused features are then used for classification. Detailed descriptions of each part will be provided in the subsequent subsections.

2.1. Dataset

The dataset for this study was sourced from the Parkinson's progression marker initiative (PPMI) website (www.ppmi-info.org/), comprising 145 samples: 101 cases in the PD group and 44 cases in the HC group. PPMI is a large, open-access dataset comprised of multiple global sites, with all participants' personal information anonymized and securely stored in the PPMI sample database. Researchers must submit an application and obtain authorization to access these data.

Demographic information for both groups is provided in table 1. Those two groups were randomly partitioned into 70% for training data ($n = 102$, PD: 71, HC: 31) and 30% for testing data ($n = 43$, PD: 30, HC: 13) before each experiment. Since each sample

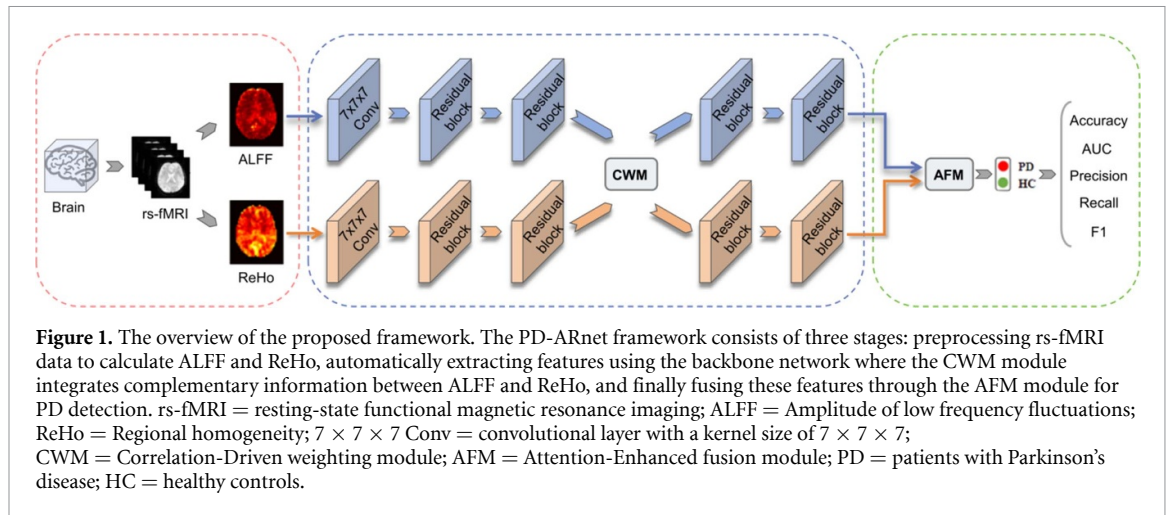


Table 1. Summary of demographic information of the HC and PD patients in this study.

Groups	Age (Years, mean \pm SD)	Gender
PD	63.0 \pm 9.7	M 66/F 35
HC	63.6 \pm 11.1	M 31/F 13
Group difference statistics	$t = 0.30, p = 0.77$	$\chi^2 = 0.17, p = 0.68$

Note: Age differences were tested using independent-sample t -test, gender differences were tested using a Chi-squared test, $p > 0.05$ indicates no statistically significant difference between the two groups. M = male; F = female; HC = healthy controls; PD = Parkinson's disease subjects.

is associated with both ALFF and ReHo image data, a total of 290 3D images were divided into 204 training images and 86 testing images for deep learning.

The rs-fMRI scanning parameters were as follows: Manufacturer = SIEMENS, Field Strength = 3.0 tesla, Pulse Sequence = EP, Repetition Time = 2400.0 ms, Echo Time = 25.0 ms, Flip Angle = 80.0 degrees, Matrix X = 476.0 pixels, Matrix Y = 462.0 pixels, Pixel Spacing X = 3.3 mm, Pixel Spacing Y = 3.3 mm, Slice Thickness = 3.3 mm, Slice Number = 40, Time Points = 210.

2.2. Data preprocessing

The preprocessing of rs-fMRI data was performed using the DPABI software (<http://rfmri.org/dpabi>) [26]. The preprocessed data were used for ALFF and ReHo calculations. The main preprocessing steps included: (1) Removing the first 10 time points to stabilize the magnetization of the machine. (2) Slice time correction was applied, ensuring synchronization of all scan layers to acquire data simultaneously. (3) Head movement correction was implemented to mitigate interference resulting from subjects' head movements during the test. (4) Spatial kernel normalization was utilized to register the fMRI images with the EPI template, ensuring precise data alignment across different subjects. (5) Linear and quadratic trends were removed to minimize the impact of noise and artifacts, enhancing data stability.

2.3. ALFF and ReHo calculation

For the ALFF calculation, first, a fast Fourier transform was used to convert the filtered time series

to a frequency domain to obtain the power spectrum. Then, the power spectrum was then square-rooted and averaged across 0.01–0.1 Hz at each voxel. For the ReHo calculation, first, the data preprocessed was filtered at 0.01–0.1 Hz. Then, Kendall's Coefficient of Concordance was applied to calculate the similarity between a single voxel and the surrounding 27 voxels.

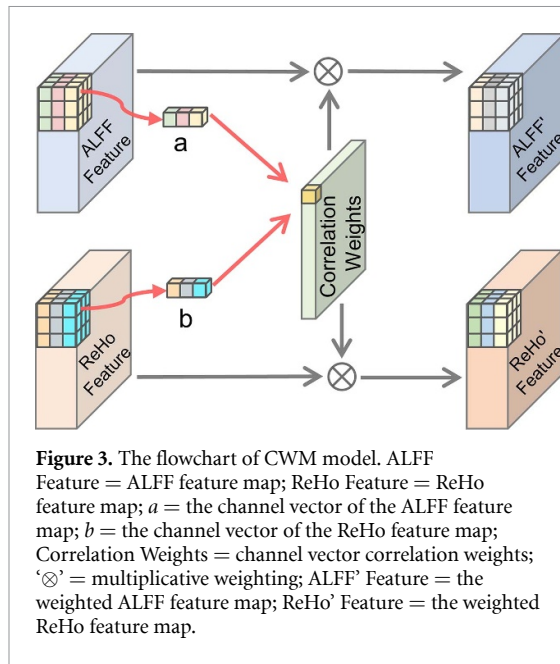
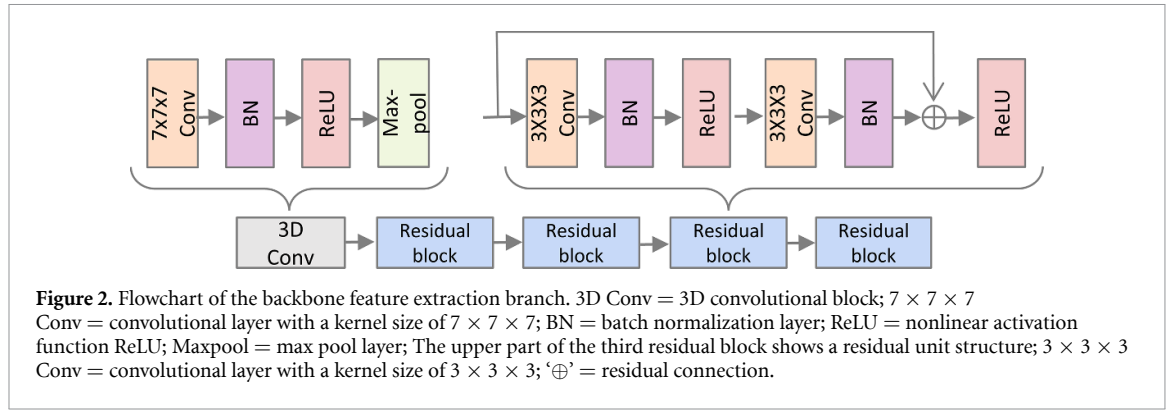
2.4. Data augmentation

Since the number of PD samples in the training set is larger than that of HC samples, the model may tend to focus on learning PD features while neglecting HC features during training. To address this, we applied data augmentation to the HC group by randomly scaling each HC sample's ALFF and ReHo images by a factor of 1.2–1.5. As the number of PD samples is sufficient to support effective model training, we did not perform additional data augmentation on the PD group to reduce data redundancy and lighten the model's training burden.

Data augmentation increases the diversity of training data through random scaling transformations, preventing the model from memorizing specific details. This helps to alleviate classification interference caused by sample imbalance and reduces the risk of overfitting during model training, thereby enhancing the generalization ability and robustness to noise of the model [27].

2.5. Feature extraction branch

The backbone feature extractor in PD-ARnet includes two extraction branches, both constructed based on



3D Resnet. These branches are used to extract two types of features, ALFF and ReHo, respectively. Each branch consists of a 3D convolutional block and four 3D residual blocks. The 3D convolutional block consists of a convolutional layer with a kernel size of $7 \times 7 \times 7$, a batch normalization layer, a ReLU layer, and a MaxPool layer. Within each 3D residual block are two residual units, where each residual unit contains a convolutional layer with a kernel size of $3 \times 3 \times 3$, a batch normalization layer, and a ReLU layer. The flowchart of backbone feature extraction branch is shown in figure 2.

2.6. Correlation-Driven weighting module (CWM)

To capture the similarities and differences between ALFF and ReHo in the feature extraction process, and effectively leverage their complementary relationship, we developed the CWM module. This module calculates channel vector correlation weights for each pixel in the same spatial position of the two feature maps, and multiply the two feature maps by these weights for weighting. The flowchart of CWM module is shown in figure 3.

The calculation process of correlation in the CWM module follows these steps:

- (1) Calculate the average of the two feature maps on their respective channel dimensions separately. The calculation process is shown in equation (1), where Feature_c is the individual pixel values of the feature map on the c th channel,

$$\text{Mean} = \frac{1}{c} \sum_{c=1}^c \text{Feature}_c \quad (1)$$

- (2) Centralize the two feature maps separately. The calculation process is shown in equation (2). Where Feature is the feature map and Mean is the average value of the feature map,

$$\text{Feature}_{\text{centered}} = \text{Feature} - \text{Mean} \quad (2)$$

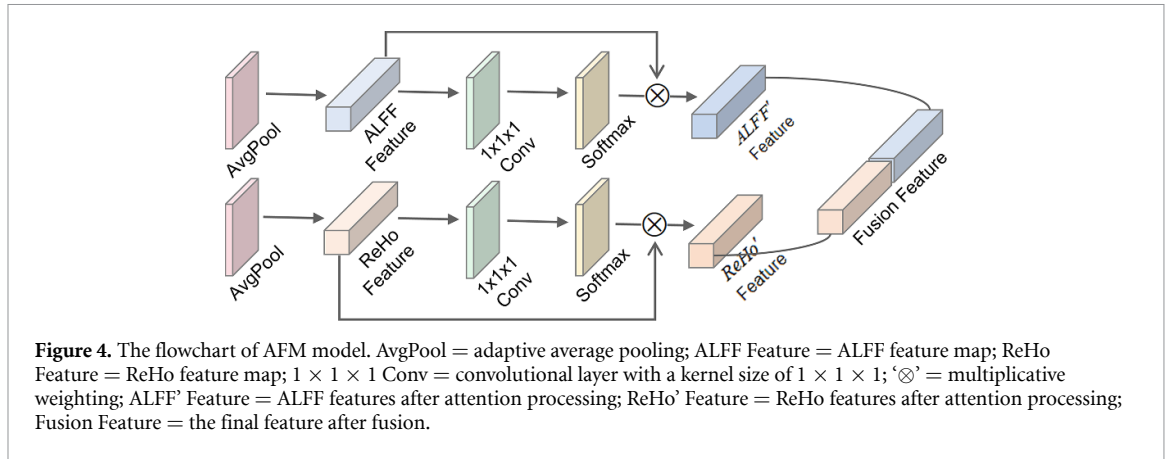
- (3) Calculate the covariance matrix of the two feature maps. The calculation process is shown in equation (3). Where $\text{ALFF}_{\text{centered},c}$ and $\text{ReHo}_{\text{centered},c}$ is the values of the two feature maps after centralization on the c th channel, respectively,

$$\text{Cov} = \frac{1}{c} \sum_{c=1}^c \text{ALFF}_{\text{centered},c} \times \text{ReHo}_{\text{centered},c} \quad (3)$$

- (4) Calculate the standard deviation of the two feature maps separately. The calculation process is shown in equation (4). Where $\text{Feature}_{\text{centered},c}$ is the feature map values after centralization on the c th channel,

$$\text{Feature}_{\text{std}} = \sqrt{\frac{1}{c} \sum_{c=1}^c (\text{Feature}_{\text{centered},c})^2} \quad (4)$$

- (5) Compute the correlation between the two feature maps. The calculation process is shown in equation (5). Where Cov is the covariance matrix of the two feature maps, ALFF_{std} and ReHo_{std} is the standard deviation of the two feature maps,



ε is a very small positive number to prevent the error that the divisor is 0,

$$\text{Correlation} = \frac{\text{Cov}}{\text{ALFF}_{\text{std}} \times \text{ReHo}_{\text{std}} + \varepsilon}. \quad (5)$$

Subsequently, the weighted feature maps ALFF' and ReHo' are obtained by multiplying the correlation weights with the corresponding original feature maps.

Although ALFF' and ReHo' contain both complementary relationship information, there are still differences in their expression, information content, and local region relationships. To address this, it is essential to pass them through the subsequent two residual blocks for advanced feature extraction, so that the model can learn more complex brain activity patterns and structures.

2.7. Attention-Enhanced fusion module (AFM)

To fully leverage the extracted ALFF and ReHo features for classification, we developed the AFM module. This module fuses ALFF and ReHo features using attention mechanisms, so that the features with the greatest contribution to classification can be highlighted in the fusion features. The flowchart of AFM module is shown in figure 4.

Initially, the inter-channel correlations are calculated by multiplying the feature map with its transpose matrix in channel dimension after adaptive average pooling. Subsequently, a 3D convolutional layer with a kernel size of $1 \times 1 \times 1$ is employed to learn the inter-channel relationships, facilitating linear transformations between channels. Finally, a softmax function is used to obtain channel importance weights by exponentiating and normalizing the results along the channel dimension. These weights are then multiplied by the feature map for channel attention weighting.

Following the channel attention weighting, the two types of enhanced feature maps are concatenated along the channel dimension, achieving the fusion of ALFF and ReHo features.

2.8. Classifier and loss function

The classifier consists of a fully connected (FC) layer and a softmax layer. First, the feature map output by the AFM module is flattened into a one-dimensional vector, and fed into the FC layer. Then, linear transformations are conducted in FC using weight matrices and bias vectors, mapping the input data to different classes in the output space. The FC calculation process is illustrated in equation (6), where x is the input vector, w_i is the weight coefficients of the FC layer, x_i is the value of the i th neuron, and b_i is the bias vector,

$$y_{w,b}(x) = f\left(\sum_{i=1}^n w_i x_i + b_i\right). \quad (6)$$

Finally, the softmax layer is applied to map the output into a probability distribution, representing the probabilities of classification as PD or HC.

In PD-ARnet, the cross-entropy function was adopted as the loss function for guiding the training process. The calculation process is depicted in equation (7), where y is the true labels of the samples (1 for PD, 0 for HC), and \hat{y} is the probability value of PD predicted by the model,

$$\text{Loss} = -[y \log \hat{y} + (1 - y) \log (1 - \hat{y})]. \quad (7)$$

During the backpropagation process, the Adam optimizer is employed to update weights and biases, facilitating the model to minimize the loss function and achieve superior classification performance.

2.9. Deep learning feature visualization

In order to enhance the interpretability of deep learning methods, we employed the 3D Grad-CAM technique to visualize the brain regions contributing most to the classification under the perspective of PD-ARnet. 3D Grad-CAM is an improvement upon Grad-CAM [28], designed for visualizing 3D images. The core principle involves performing a forward pass with pre-trained parameters, generating a one-hot

tensor matching the output shape, obtaining gradient information for the target category through back-propagation of the one-hot tensor, and ultimately calculating weights based on this gradient information. The calculation process is depicted in equation (8), where α_k^c is the weight of channel k in the target class c , (d, h, w) is the depth, height, and width of the feature map respectively, y^c is the probability associated with the target class c in the output, and A_{dhw}^k is the activation value at the position (d, h, w) in the k th channel,

$$\alpha_k^c = \frac{1}{d \times h \times w} \sum_d \sum_h \sum_w \frac{\partial y^c}{\partial A_{dhw}^k}. \quad (8)$$

Finally, the feature maps were weighted and summed according to their respective weights, and the ReLU activation function was used to set the negative gradient pixels to 0 to obtain the final heat map. The calculation process is depicted in equation (9),

$$L_{3DGrad-CAM}^c = \text{ReLU} \left(\sum_k \alpha_k^c A^k \right). \quad (9)$$

By employing the 3D Grad-CAM module, we can visualize the attention regions of PD-ARnet, aiding in understanding the focal points during the decision-making process. This is crucial for the deep learning model interpretation and exploration of potential new biomarkers for PD.

2.10. Ablation experiments

Ablation experiments were conducted to verify the overall superiority of PD-ARnet. Firstly, single-branch classification networks, namely PD-net-A (using only ALFF as input) and PD-net-R (using only ReHo as input), are constructed based on 3D ResNet to assess the classification performance of single-branch models under individual parameter input conditions. Subsequently, the AFM module was utilized to merge PD-net-A and PD-net-R, resulting in the creation of the dual-branch classification network called PD-funet. This network took both ALFF and ReHo parameters as inputs and evaluated the model's performance using fused features. Lastly, the CWM module was introduced into PD-funet to validate the complete PD-ARnet's classification performance after integrating dual-branch information during the feature extraction process.

2.11. Model implementation details

The model is implemented in Python 3.8.5 and Pytorch 1.12.1 library and trained with NVIDIA Tesla P100 GPU using CUDA 10.2 on Ubuntu 16.04.7 operating system. The model was utilized a binary cross-entropy loss function, with a batch size of 32. We set the initial learning rate to 1×10^{-4} and applied a learning rate decay strategy, whereby the learning rate is reduced to 90% of its original value every 5 epochs. This learning rate decay strategy gradually

decreases the magnitude of parameter updates in the deep learning model, thereby reducing the risk of overfitting on the training set and aiding the model in finding the global optimum solution [29].

2.12. Evaluation and statistical analysis

All models underwent 10 experiments, with random allocation of training and testing sets before each experiment. The average, standard deviation, and 95% confidence interval of accuracy, precision, recall, F1 score, and AUC were then calculated.

The statistical and deep learning analyses were performed using Python (version 3.8.5) software. Paired t -tests were utilized to assess the differences in each evaluation metric for every model across ten experiments, and $p < 0.05$ indicated a statistically significant result.

3. Results

3.1. Performance of PD-ARnet

The changes of the average accuracy, precision, recall, and F1 score of PD-ARnet on the test set across training epochs are shown in figure 5(a). Meanwhile, the average loss curve on the test set is shown in figure 5(b). It is evident that all four average evaluation metric curves show a gradual increase as the progress of training. There is a noticeable increase between the 10th and 15th epochs, followed by a slowdown in the increment between the 15th and 25th epochs. Between the 25th and 35th epochs, the increment stabilizes, and the curves tend to plateau. Additionally, the average loss curve demonstrates a gradual decrease over the training epochs. This indicates that PD-ARnet gradually learned the crucial information within ALFF and ReHo that can be used to distinguish between PD and HC. The ROC curves of PD-ARnet on the test set across 10 experiments are shown in figure 5(c), while figure 5(d) illustrates the average classification accuracy, precision, recall, F1 score, and AUC, reaching 0.916 ± 0.012 , 0.947 ± 0.007 , 0.862 ± 0.020 , 0.902 ± 0.014 and 0.928 ± 0.031 , respectively.

3.2. Performance of different ablation models

The results of the classification evaluation metrics for the different models on the test set are presented in table 2. The classification performance of PD-net-A is comparable to PD-net-R on the five evaluation metrics. Compared with PD-net-A, PD-funet demonstrated significant improvements in accuracy (0.888 vs. 0.851), precision (0.928 vs. 0.907), recall (0.818 vs. 0.756), F1 score (0.869 vs. 0.824), and AUC (0.890 vs. 0.851). Likewise, compared with PD-net-R, PD-funet demonstrated significant improvements in accuracy (0.888 vs. 0.853), precision (0.928 vs. 0.886), recall (0.818 vs. 0.777), F1 score (0.869 vs. 0.826), and displayed an improvement, although not significantly in AUC (0.890 vs. 0.872, $p = 0.195$). Moreover,

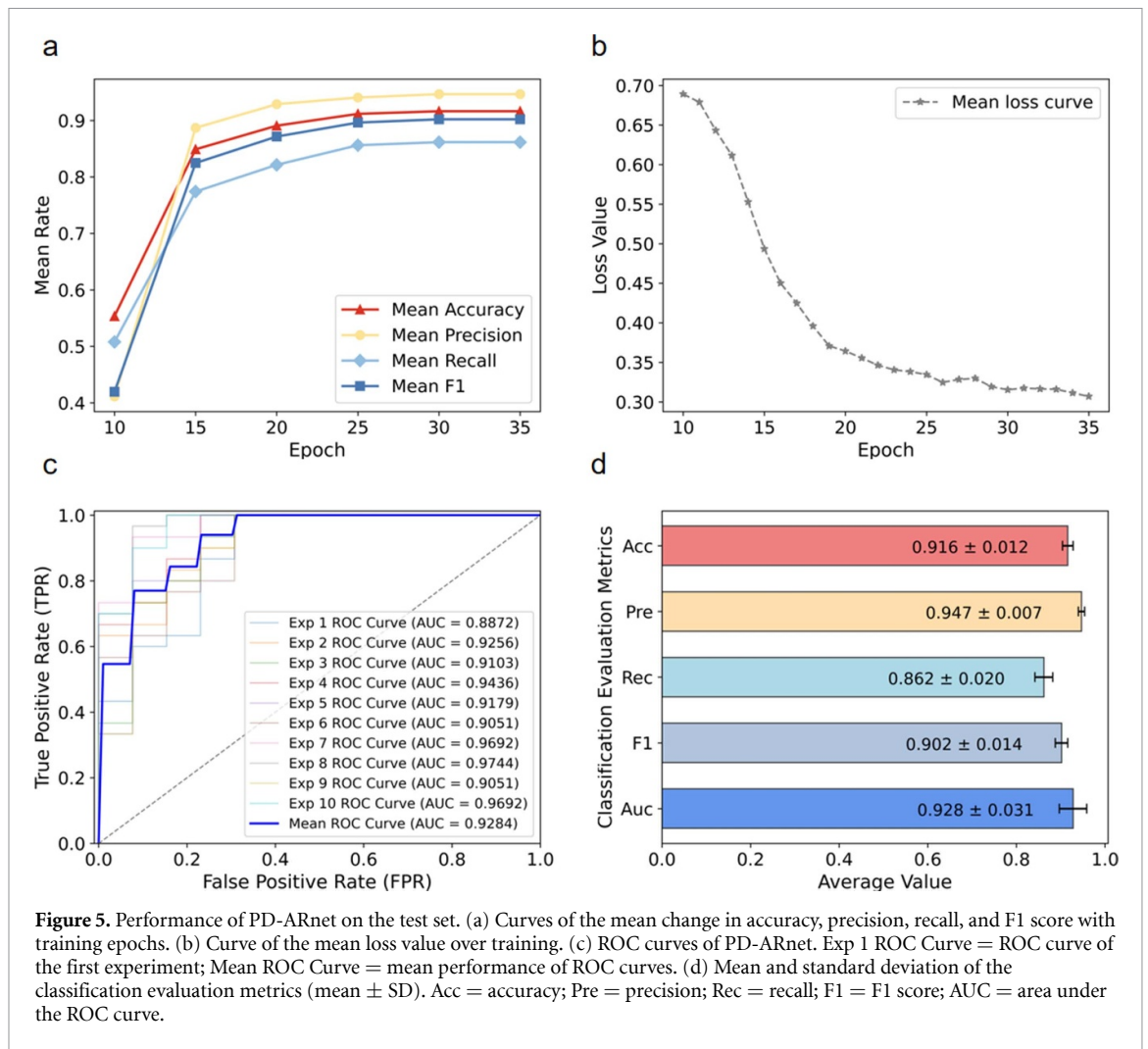


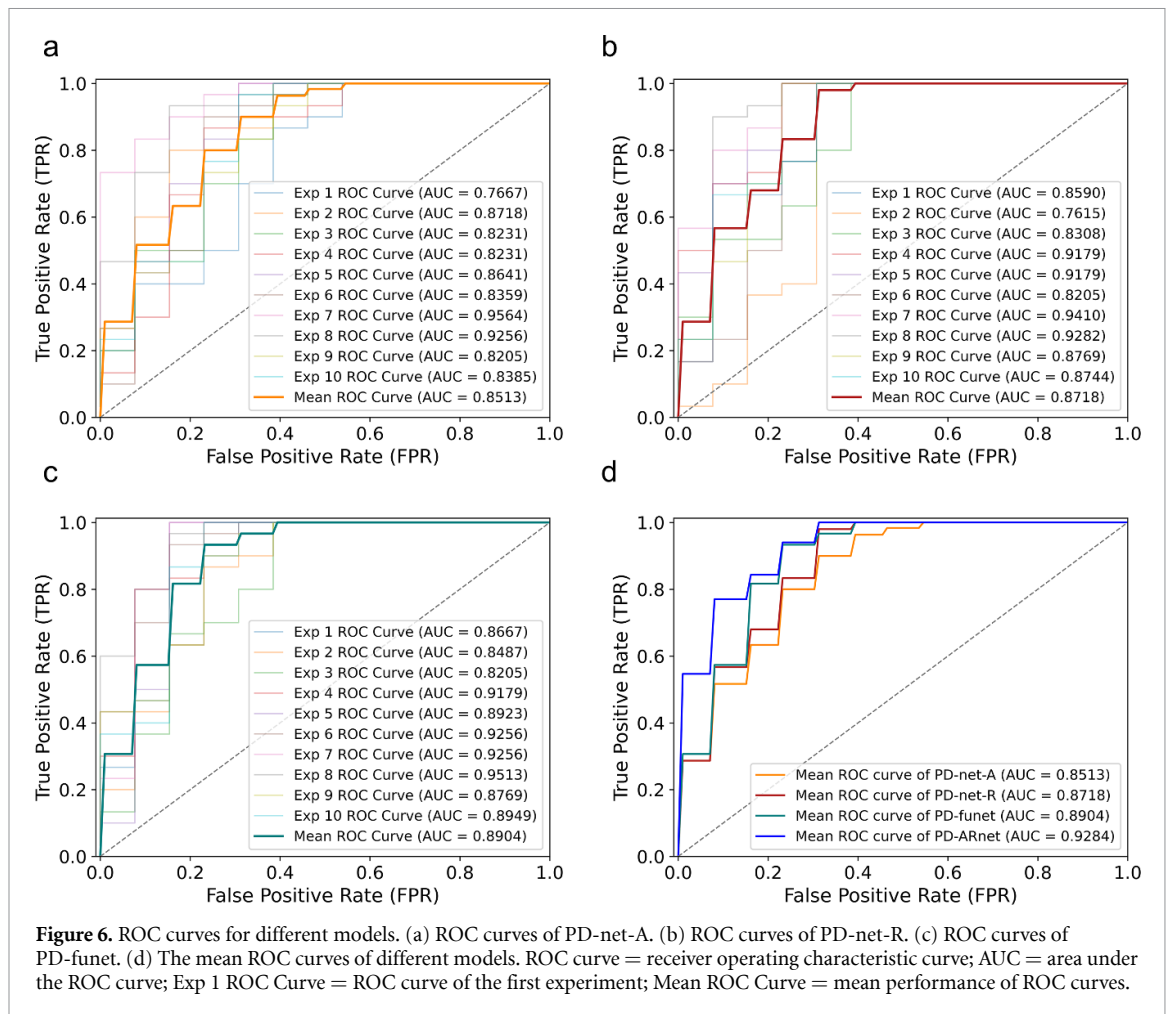
Table 2. The evaluation metrics results for different models on the test set.

Model	Accuracy	Precision	Recall	F1 score	AUC
PD-net-A	0.851 [0.832,0.871] $p2 < 0.001$	0.907 [0.892,0.923] $p2 = 0.038$	0.756 [0.724,0.788] $p2 < 0.001$	0.824 [0.801,0.848] $p2 < 0.001$	0.851 [0.818,0.887] $p2 = 0.029$
PD-net-R	0.853 [0.830,0.877] $p2 = 0.007$	0.886 [0.860,0.912] $p2 = 0.021$	0.777 [0.733,0.821] $p2 = 0.034$	0.826 [0.798,0.854] $p2 = 0.006$	0.872 [0.838,0.908] $p2 = 0.195$
PD-funet	0.888 [0.875,0.902] $p1 < 0.001$	0.928 [0.920,0.936] $p1 = 0.002$	0.818 [0.794,0.841] $p1 = 0.002$	0.869 [0.851,0.889] $p1 < 0.001$	0.890 [0.887,0.926] $p1 = 0.005$
PD-ARnet	0.916 [0.909,0.924]	0.947 [0.942,0.951]	0.862 [0.849,0.874]	0.902 [0.893,0.911]	0.928 [0.911,0.950]

Note: Each evaluation metric is presented as the mean value, [] shows the 95% confidence interval. $p1$ represents the comparison with the corresponding metric in PD-ARnet, and $p2$ represents the comparison with the corresponding metric in PD-funet. Bolded values indicate the optimal performance for the respective evaluation metric.

when compared with PD-funet, PD-ARnet demonstrated significant improvements in accuracy (0.916 vs. 0.888), precision (0.947 vs. 0.928), recall (0.862 vs. 0.818), F1 score (0.902 vs. 0.869), and AUC (0.928 vs. 0.890).

Furthermore, the ROC curves of the different models are shown in figure 6. It was obvious that PD-ARnet achieved the best discrimination performance based on the mean ROC curve, followed by the PD-funet.



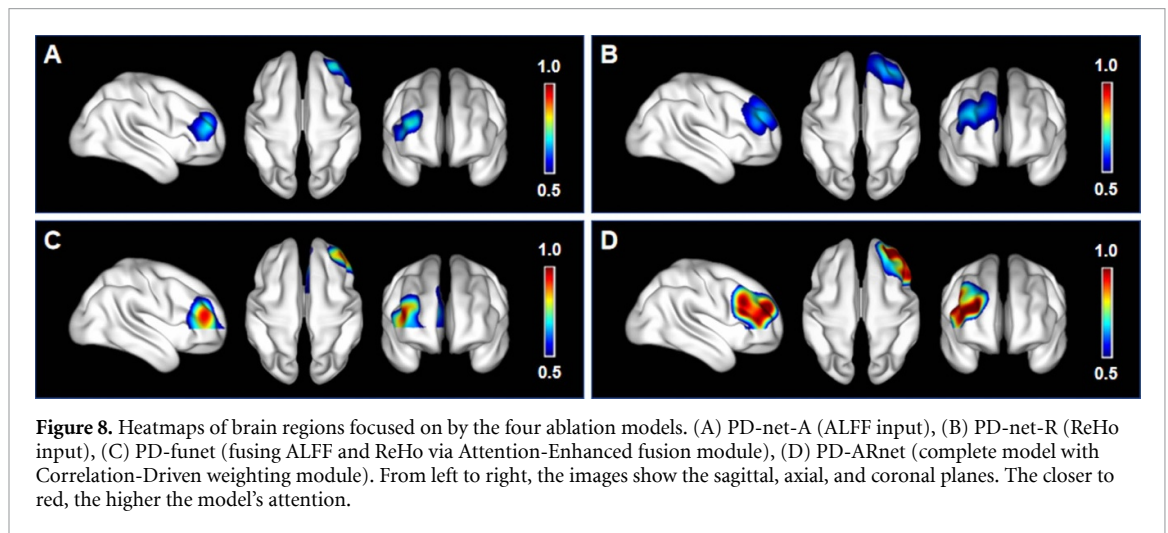
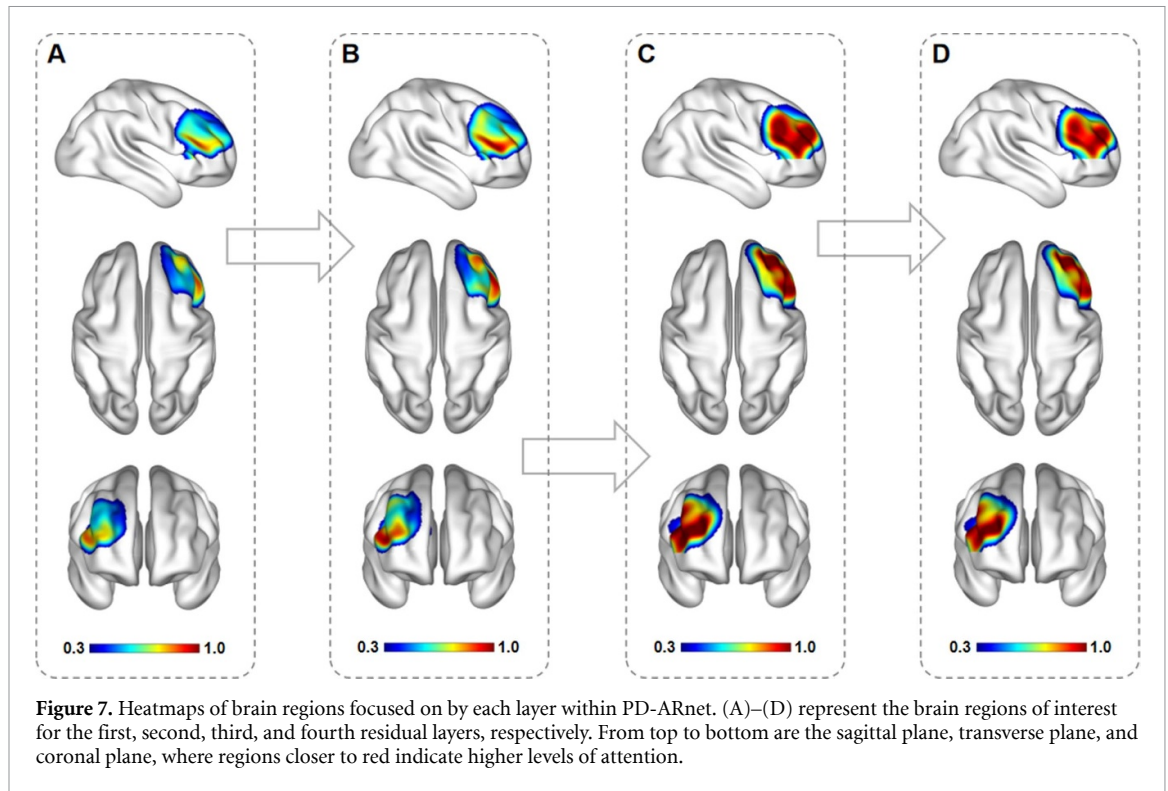
3.3. Qualitative analysis

To explain and understand the internal working mechanism and decision-making process of the model, we performed a layer-by-layer feature visualization within the model. Additionally, we visualized the regions of focus for different ablation models to evaluate the contribution of each module and the overall design's validity.

The layer-by-layer changes in the regions of focus for the four residual layers (Each residual layer includes two parallel residual blocks) in PD-ARnet are shown in figure 7. As the model depth increases, the focus gradually expands from localized regions in the prefrontal cortex to broader areas in the motor cortex. Specifically, the first layer focuses on a small localized area within the prefrontal cortex. The prefrontal cortex plays a crucial role in the pathology of PD [30], and this focus reflects the model's ability to identify important features related to PD pathology at an early stage. The second layer's focus extends to the supplementary motor area, indicating that the model begins to integrate features related to motor function. The third layer further expands the focus to cover a wider area of the motor cortex, suggesting that the model is synthesizing more advanced

and complex PD-related features. By the fourth layer, although the focus is similar to that of the third layer, it becomes slightly narrower with clearer boundaries, indicating that the model has fine-tuned its selection of key features, reducing attention to redundant information. This progressive change in focus areas illustrates the model's full process from initial feature capture to final refined classification decisions, ensuring the accuracy and reliability of the classification results.

The heatmaps of the brain regions focused on by the four ablation models are shown in figure 8. Specifically, the single-branch PD detection models, PD-net-A and PD-net-R, which use ALFF or ReHo as the sole input, both focus on the prefrontal cortex, with PD-net-R covering a slightly broader area. However, both models exhibit low attention levels, indicating that relying on a single feature input limits the extraction of key discriminative features. In contrast, the dual-branch PD detection model PD-funet, which fuses the two features using the AFM, shows a higher focus in localized regions of the frontal cortex. This suggests that the fusion module effectively enables the model to extract key features for PD detection. However, PD-funet's focus area, while similar



to the ALFF-only model, does not fully capture the focus seen with ReHo alone, indicating a loss of complementary information that reduces the richness of the fused features. In comparison, the complete PD-ARnet model, which incorporates the CWM into PD-funet, not only significantly enhances the focus area but also covers a broader range of brain regions. This indicates that PD-ARnet effectively utilizes the complementary information between ALFF and ReHo, capturing more features with strong discriminative power for PD.

3.4. Comparison of existing methods

We compared recent PD auxiliary diagnostic methods reported on the PPMI dataset and summarized the results in table 3.

Traditional machine learning methods like cmcRVFL+, LLCFS, and EKM+SPL depend on manual feature selection in PD diagnosis, limiting their ability to capture essential latent features and complex nonlinear relationships. In contrast, PD-ARnet, as a deep learning model, automatically learns and captures these intricate patterns, utilizing fMRI data more effectively for PD detection and outperforming traditional methods across various metrics. Although Cross-GNN and BrainMass also use deep learning with fMRI data, their complex architectures (e.g. Graph Neural Networks and Transformer Encoders) may lead to longer training times and lower inference efficiency. PD-ARnet's straightforward feature extraction and fusion approach preserves the strong feature learning capabilities of deep

Table 3. Comparison of other reported methods on the PPMI dataset.

Model	Accuracy	Precision	Recall	F1 score	AUC
cmcRVFL+ [16]	0.819	0.743	0.827	0.781	—
LLCFS [15]	0.875	—	0.850	—	0.900
EKM+SPL [17]	0.853	0.892	0.801	—	0.842
Cross-GNN [23]	0.849	—	0.866	—	—
BrainMass [24]	0.845	—	0.827	—	—
PD-ARnet	0.916	0.947	0.862	0.902	0.928

Note: ‘—’ indicates that this metric was not reported in the study, and bold indicates the optimal metric value.

learning while enhancing efficiency. Despite Cross-GNN’s recall rate being 0.004 higher, its smaller PD patient sample size ($n = 56$) may limit its generalizability and result stability. Overall, the proposed method has achieved relatively excellent results and outperforms similar methods in terms of overall performance.

4. Discussion

In this study, we developed a deep learning model called PD-ARnet based on rs-fMRI data. The model integrates information from ALFF and ReHo, providing a valuable reference from rs-fMRI for accurate PD diagnosis. Our results demonstrate that the proposed method exhibits a high discrimination capability, suggesting its potential as an auxiliary diagnostic tool for PD.

In previous PD detection studies, traditional machine learning methods often relied on manual feature selection to construct feature engineering. However, this approach is typically limited to selecting local features, which can result in the loss of global information and subsequently impact the model’s performance [15–17]. In contrast, PD-ARnet, a deep learning model specifically designed for PD diagnosis, automates the feature extraction process, eliminating the need for manual feature selection and reducing the time required for diagnosis. PD-ARnet gradually learns high-level features that are more conducive to PD detection from global data during training. This automated learning not only enhances classification efficiency but also ensures the integrity of the information. To clearly demonstrate the effectiveness of PD-ARnet’s automated feature learning, we plotted the average curves of four classification evaluation metrics and the loss value on the test set over the training epochs. The results show that the average values of the four metrics on the test set rapidly increased in the early stages of training and then gradually stabilized, while the average loss value showed a gradual downward trend. These trends clearly indicate that PD-ARnet effectively transitions during training from learning basic features to more complex and discriminative features, thereby enhancing its generalization ability on the test set and significantly improving classification performance.

Previous deep learning methods for PD diagnosis have predominantly focused on using MRI data [16, 21, 31, 32]. However, MRI primarily captures morphological changes in various tissue types and is mainly used in PD diagnosis to exclude other diseases and reveal some structural changes, making it not the most sensitive tool for PD detection [33]. In contrast, rs-fMRI detects hemodynamic responses related to neural activity, capturing functional changes that MRI cannot reveal, which is crucial for identifying neurodegenerative changes in PD. Despite the clear advantage of rs-fMRI in providing functional information, the complexity of its four-dimensional data makes it challenging for existing deep learning methods to directly extract features effectively, limiting its widespread application. In this context, this study proposes PD-ARnet, a method that leverages two three-dimensional features, ALFF and ReHo, extracted from rs-fMRI, to achieve effective PD detection and classification. PD-ARnet automates the learning and integration of ALFF and ReHo functional information, not only overcoming the challenges of processing four-dimensional data but also significantly improving the accuracy and robustness of PD detection. The results demonstrate that PD-ARnet achieves higher precision and reliability in PD diagnosis using rs-fMRI, providing new insights for future PD detection based on rs-fMRI and showing its broad clinical application potential.

In previous multi-branch disease diagnosis models, the extraction of different features was often conducted independently [34–37]. This approach tends to overlook the potential complementary relationships between these features, which significantly reduces the amount of information in the fused features. Such limitations constrain the model’s potential in disease diagnosis. To address this issue, we introduced the specifically designed CWM module in our study, with the aim of capturing the complementary information between ALFF and ReHo features. To validate the module’s effectiveness, we conducted ablation experiments. The results demonstrated that the complete PD-ARnet model, which incorporates the CWM module into the independent dual-branch model, achieved the best classification performance. This indicates that the CWM

module effectively enables the model to capture the synergy between ALFF and ReHo, allowing it to extract more comprehensive and enriched feature representations, ultimately enhancing the model's PD detection performance. This finding further reveals the complexity and diversity of functional changes in PD patients, offering new insights into understanding the neuropathological mechanisms of PD. Additionally, the approach of considering the complementary relationships between different features in deep learning model design provides a new direction for developing more accurate and robust disease detection models in the future.

To enhance the interpretability of PD-ARnet, we visualized the brain regions prioritized by the model using 3D Grad-CAM, revealing a focus on the frontal lobe. While traditional studies emphasize that PD lesions primarily occur in the basal ganglia, particularly the substantia nigra, recent research indicates that PD also affects other brain regions, including the frontal lobe, which plays a crucial role in cognitive functions and motor control [38–40]. Moreover, recent studies employing machine learning and deep learning for PD detection have also highlighted abnormalities in the frontal lobe, emphasizing its significance in distinguishing PD [22, 41]. Therefore, our model's focus on this region complements existing knowledge of PD pathology, underscoring the broader impact of the disease across multiple brain regions.

Addressing bias mitigation in deep learning for medical imaging is imperative for achieving equitable and reliable healthcare outcomes. In this study, to mitigate potential biases, we first applied data augmentation techniques to balance the training set, thereby reducing bias introduced by disparities in the number of PD and HC samples. Secondly, to avoid bias in the model's predictions due to specific age or gender distributions in any single training set division, we used random training sets for multiple training iterations. This bias mitigation strategy ensures that the model generalizes well across different data subsets. These steps aim to reduce the impact of bias factors and enhance the reliability and fairness of deep learning applications in healthcare.

4.1. Limitations and future directions

While this study has yielded promising results, it is important to address potential limitations and outline future research directions. First, the relatively small sample size may limit the generalizability of the findings. Future studies should validate the model using larger and more heterogeneous datasets to ensure broader applicability. Additionally, while our model has demonstrated effectiveness in integrating ALFF and ReHo features, future research could enhance performance by exploring other deep learning architectures, such as ConvNeXt and

RepVGG, which have recently gained significant recognition in pattern recognition. Furthermore, incorporating additional biomarkers, including various imaging data from advanced neuroimaging techniques, could lead to a more comprehensive understanding of PD through the integration of multimodal data. Continued research in these areas will be crucial for refining the model and advancing its clinical utility.

5. Conclusion

In summary, this study developed a deep learning model utilizing ALFF and ReHo extracted from rs-fMRI data for the detection of PD. The results demonstrate that the proposed model exhibits excellent discriminatory performance. This finding can serve as a valuable reference for clinicians in the diagnosis of PD and may help alleviate the burden on less experienced doctors during the diagnostic process.

Data availability statement

The data that support the findings of this study are openly available at the following URL/DOI: www.ppmi-info.org/access-data-specimens/download-data.

Funding information

This work was supported by Henan Province Science and Technology R&D Project (No. 242102210042); Henan Province Science and Technology R&D Project (No. 232102210029); Kaifeng Science and Technology R&D Project (No. 2201009)

Conflict of interest

The authors have no financial or proprietary interests in any material discussed in this article.

ORCID iD

Yalin Song  <https://orcid.org/0009-0002-4034-2286>

References

- [1] Kalia L V and Lang A E 2015 Parkinson's disease *Lancet* **386** 896–912
- [2] Rizzo G, Copetti M, Arcuti S, Martino D, Fontana A and Logroscino G 2016 Accuracy of clinical diagnosis of Parkinson disease: a systematic review and meta-analysis *Neurology* **86** 566–76
- [3] Moscovich M, Heinzel S, Postuma R B, Reilmann R, Klockgether T, Jacobi H, Höglinger G and Berg D 2020 How specific are non-motor symptoms in the prodrome of Parkinson's disease compared to other movement disorders? *Parkinsonism Relat. Disorders* **81** 213–8
- [4] Tolosa E, Garrido A, Scholz S W and Poewe W 2021 Challenges in the diagnosis of Parkinson's disease *Lancet Neurol.* **20** 385–97

- [5] Postuma R B and Berg D 2016 Advances in markers of prodromal Parkinson disease *Nat. Rev. Neurol.* **12** 622–34
- [6] Mantri S, Morley J F and Siderowf A D 2019 The importance of preclinical diagnostics in Parkinson disease *Parkinsonism Relat. Disorders* **64** 20–28
- [7] Vivar-Estudillo G et al 2021 Parkinson's disease detection and diagnosis from fMRI: a literature review *Int. Conf. on Human-Computer Interaction* (Springer International Publishing)
- [8] Xu N, Zhou Y, Patel A, Zhang N and Liu Y 2023 Parkinson's disease diagnosis beyond clinical features: a bio-marker using topological machine learning of resting-state functional magnetic resonance imaging *Neuroscience* **509** 43–50
- [9] Zuo X-N and Xing X-X 2014 Test-retest reliabilities of resting-state fMRI measurements in human brain functional connectomics: a systems neuroscience perspective *Neurosci. Biobehav. Rev.* **45** 100–18
- [10] Yu-Feng Z, Yong H, Chao-Zhe Z, Qing-Jiu C, Man-Qiu S, Meng L, Li-Xia T, Tian-Zi J and Yu-Feng W 2007 Altered baseline brain activity in children with ADHD revealed by resting-state functional MRI *Brain Dev.* **29** 83–91
- [11] Zang Y, Jiang T, Lu Y, He Y and Tian L 2004 Regional homogeneity approach to fMRI data analysis *NeuroImage* **22** 394–400
- [12] Tang Y, Meng L, Wan C-M, Liu Z-H, Liao W-H, Yan X-X, Wang X-Y, Tang B-S and Guo J-F 2017 Identifying the presence of Parkinson's disease using low-frequency fluctuations in BOLD signals *Neurosci. Lett.* **645** 1–6
- [13] Yue Y, Jiang Y, Shen T, Pu J, Lai H-Y and Zhang B 2020 ALFF and ReHo mapping reveals different functional patterns in early- and late-onset Parkinson's disease *Front. Neurosci.* **14** 141
- [14] Shi D, Yao X, Li Y, Zhang H, Wang G, Wang S and Ren K 2022 Classification of Parkinson's disease using a region-of-interest and resting-state functional magnetic resonance imaging-based radiomics approach *Brain Imaging Behav.* **16** 2150–63
- [15] Cigdem O, Demirel H and Unay D 2019 The performance of local-learning based clustering feature selection method on the diagnosis of parkinson's disease using structural MRI 2019 IEEE Int. Conf. on Systems, Man and Cybernetics (SMC) (IEEE)
- [16] Shi J, Xue Z, Dai Y, Peng B, Dong Y, Zhang Q and Zhang Y 2018 Cascaded multi-column RVFL+ classifier for single-modal neuroimaging-based diagnosis of Parkinson's disease *IEEE Trans. Biomed. Eng.* **66** 2362–71
- [17] Pang C, Zhang Y, Xue Z, Bao J, Keong Li B, Liu Y, Liu Y, Sheng M, Peng B and Dai Y 2023 Improving model robustness via enhanced feature representation and sample distribution based on cascaded classifiers for computer-aided diagnosis of brain disease *Biomed. Signal Process. Control* **79** 104047
- [18] Pan P, Zhang Y, Liu Y, Zhang H, Guan D and Xu Y 2017 Abnormalities of regional brain function in Parkinson's disease: a meta-analysis of resting state functional magnetic resonance imaging studies *Sci. Rep.* **7** 40469
- [19] Pan P, Zhan H, Xia M, Zhang Y, Guan D and Xu Y 2017 Aberrant regional homogeneity in Parkinson's disease: a voxel-wise meta-analysis of resting-state functional magnetic resonance imaging studies *Neurosci. Biobehav. Rev.* **72** 223–31
- [20] Janiesch C, Zschech P and Heinrich K 2021 Machine learning and deep learning *Electron. Markets* **31** 685–95
- [21] Vyas T, Yadav R, Solanki C, Darji R, Desai S and Tanwar S 2022 Deep learning-based scheme to diagnose Parkinson's disease *Expert Syst.* **39** e12739
- [22] Yang M, Huang X, Huang L and Cai G 2023 Diagnosis of Parkinson's disease based on 3D ResNet: the frontal lobe is crucial *Biomed. Signal Process. Control* **85** 104904
- [23] Yang Y, Ye C, Guo X, Wu T, Xiang Y and Ma T 2024 Mapping multi-modal brain connectome for brain disorder diagnosis via cross-modal mutual learning *IEEE Trans. Med. Imaging.* **43** 108–21
- [24] Yang Y, Ye C, Su G, Zhang Z, Chang Z, Chen H, Chan P, Yu Y and Ma T 2024 BrainMass: advancing brain network analysis for diagnosis with large-scale self-supervised learning *IEEE Trans. Med. Imaging* **1**
- [25] He K et al 2016 Deep residual learning for image recognition *Proc. IEEE Conf. on Computer Vision and Pattern Recognition*
- [26] Yan C-G, Wang X-D, Zuo X-N and Zang Y-F 2016 DPABI: data processing & analysis for (resting-state) brain imaging *Neuroinformatics* **14** 339–51
- [27] Connor S and Khoshgoftaar T M 2019 A survey on image data augmentation for deep learning *J. Big Data* **6** 1–48
- [28] Selvaraju R R et al 2017 Grad-cam: visual explanations from deep networks via gradient-based localization *Proc. IEEE Int. Conf. on Computer Vision*
- [29] Ismail A, Ahmad S A, Che Soh A, Hassan K and Harith H H 2019 Improving convolutional neural network (CNN) architecture (miniVGGNet) with batch normalization and learning rate decay factor for image classification *Int. J. Integr. Eng.* **11** 51–59
- [30] Rowe J, Stephan K E, Friston K, Frackowiak R, Lees A and Passingham R 2002 Attention to action in Parkinson's disease: impaired effective connectivity among frontal cortical regions *Brain* **125** 276–89
- [31] Shah P M et al 2018 Detection of Parkinson disease in brain MRI using convolutional neural network 2018 24th Int. Conf. on Automation and Computing (ICAC) (IEEE)
- [32] Bhan A et al 2021 Early diagnosis of Parkinson's disease in brain MRI using deep learning algorithm 2021 3rd Int. Conf. on Intelligent Communication Technologies and Virtual Mobile Networks (ICICV) (IEEE)
- [33] Holtbernd F and Eidelberg D 2014 The utility of neuroimaging in the differential diagnosis of parkinsonian syndromes *Seminars in Neurology* vol 34 (Thieme Medical Publishers)
- [34] Chai Y et al 2017 Deep learning through two-branch convolutional neuron network for glaucoma diagnosis *Smart Health: Int. Conf., ICSH 2017, Hong Kong, China, June 26–27, 2017, Proc.* (Springer International Publishing)
- [35] Li Y and Shen L 2018 Deep learning based multimodal brain tumor diagnosis *Brainlesion: Glioma, Multiple Sclerosis, Stroke and Traumatic Brain Injuries: 3rd Int. Workshop, BrainLes 2017, Held in Conjunction with MICCAI 2017, Quebec City, QC, Canada, September 14, 2017, Revised Selected Papers 3* (Springer International Publishing)
- [36] Khan M A, Ashraf I, Alhaisoni M, Damaševičius R, Scherer R, Rehman A and Bukhari S A C 2020 Multimodal brain tumor classification using deep learning and robust feature selection: a machine learning application for radiologists *Diagnostics* **10** 565
- [37] Cong C, Li X, Zhang C, Zhang J, Sun K, Liu L, Ambale-Venkatesh B, Chen X and Wang Y 2024 MRI-based breast cancer classification and localization by multiparametric feature extraction and combination using deep learning *J. Magn. Reson. Imaging* **59** 148–61
- [38] Kendi A K, Lehericy S, Luciana M, Ugurbil K and Tuite P 2008 Altered diffusion in the frontal lobe in Parkinson disease *Am. J. Neuroradiol.* **29** 501–5
- [39] Chaudhary S, Kumaran S S, Goyal V, Kalaivani M, Kaloiya G S, Sagar R and Jagannathan N R 2021 Frontal lobe metabolic alterations characterizing Parkinson's disease cognitive impairment *Neurol. Sci.* **42** 1053–64
- [40] Skidmore F M et al 2013 Reliability analysis of the resting state can sensitively and specifically identify the presence of Parkinson disease *NeuroImage* **75** 249–61
- [41] Pang H, Yu Z, Yu H, Cao J, Li Y, Guo M and Fan G 2021 Use of machine learning method on automatic classification of motor subtype of Parkinson's disease based on multilevel indices of rs-fMRI *Parkinsonism Relat. Disorders* **90** 65–72